



# Probing the SO<sub>2</sub> Adsorption Mechanism in Hofmann Clathrates via Inelastic Neutron Scattering and Density Functional Theory Calculations

Ángel Fernández-Blanco, Lucía Piñeiro-López, Mónica Jiménez-Ruiz, Stéphane Rols, J. Alberto Rodríguez-Velamazán, Roberta Poloni, José Antonio Real

## ► To cite this version:

Ángel Fernández-Blanco, Lucía Piñeiro-López, Mónica Jiménez-Ruiz, Stéphane Rols, J. Alberto Rodríguez-Velamazán, et al.. Probing the SO<sub>2</sub> Adsorption Mechanism in Hofmann Clathrates via Inelastic Neutron Scattering and Density Functional Theory Calculations. *Journal of Physical Chemistry C*, 2022, 126 (18), pp.8090-8099. 10.1021/acs.jpcc.2c01030 . hal-03863778

**HAL Id: hal-03863778**

**<https://hal.science/hal-03863778>**

Submitted on 21 Nov 2022

**HAL** is a multi-disciplinary open access archive for the deposit and dissemination of scientific research documents, whether they are published or not. The documents may come from teaching and research institutions in France or abroad, or from public or private research centers.

L'archive ouverte pluridisciplinaire **HAL**, est destinée au dépôt et à la diffusion de documents scientifiques de niveau recherche, publiés ou non, émanant des établissements d'enseignement et de recherche français ou étrangers, des laboratoires publics ou privés.

# Probing the SO<sub>2</sub> adsorption mechanism in Hofmann clathrates via inelastic neutron scattering and density functional theory calculations

Ángel Fernández-Blanco,<sup>†,‡</sup> Lucía Piñeiro-López,<sup>¶</sup> Mónica Jiménez-Ruiz,<sup>†</sup> Stephane Rols,<sup>†</sup> José Antonio Real,<sup>§</sup> J. Alberto Rodríguez-Velamazán,<sup>\*,†</sup> and Roberta Poloni<sup>\*,||</sup>

<sup>†</sup>*Institut Laue Langevin, 71 Avenue des Martyrs, CS 20156-38042, Grenoble, France*

<sup>‡</sup>*SIMaP, University of Grenoble-Alpes, 38042 Grenoble, France*

<sup>¶</sup>*IMDEA Nanociencia, Faraday 9, Ciudad Universitaria de Cantoblanco, 28049 Madrid, Spain*

<sup>§</sup>*Departamento de Química Inorgánica, Instituto de Ciencia Molecular (ICMol), Universidad de Valencia, Spain*

<sup>||</sup>*Grenoble-INP, SIMaP, University of Grenoble-Alpes, CNRS, 38042 Grenoble, France*

Received February 4, 2022; E-mail: velamazán@ill.eu; roberta.poloni@grenoble-inp.fr

**Abstract:** The adsorption mechanism of SO<sub>2</sub> in the Hofmann-like coordination polymer Fe(pz)[Pt(CN)<sub>4</sub>] is studied using inelastic neutron scattering and density functional theory calculations. We find that the most important spectral change upon gas adsorption is the blueshift of the low energy peak found at 100 cm<sup>-1</sup>, a feature that is fully confirmed by the computed neutron-weighted phonon density of states. Our calculations suggest that the origin of this change is twofold: i) an increase in the force constant of the cyanide out-of-plane movement due to the binding of the gas onto the Pt(CN)<sub>4</sub> plane, and ii) the hampered rotation of the pyrazine due to steric hindrance. The high energy region of the neutron scattering data whose spectral weight is dominated by the internal vibrations of the pyrazine is negligibly affected by the presence of the gas as expected from a physisorption type of binding.

## Introduction

Metal-organic frameworks (MOFs) are 3D nanoporous materials formed through coordination bonds between metal cations and organic ligands. The great variety of metal ions, organic linkers, combined with the structural topology, allow to achieve an almost infinite number of possible combinations. Owing to this exceptional tunability, combined with the larger surface area and nanoscale porosity, the past 10-15 years have seen a rapid development in the field of MOFs for efficient gas adsorption and separation.<sup>1,2</sup> In recent years, adsorption and chemical sensing of toxic gas molecules using MOFs has become a very active field of research.<sup>3-5</sup> Among these, iron (II) spin-crossover Hofmann-type clathrates represent an interesting class of MOFs with sensing capabilities due to their bistability, meaning that they can be *switched* between two different spin states.<sup>6,7</sup> These complexes undergo a spin-state change under the influence of external stimuli such as light, temperature, pressure or the incorporation of guest molecules. A relevant feature is the presence of metallic centers with an “open” metal coordination, i.e. metal centers exhibiting an unsaturated coordination. Interestingly, these open-metal sites have been shown to exhibit a high affinity for many gases, such as CO<sub>2</sub>,<sup>8</sup> CH<sub>4</sub>,<sup>9</sup> and CO.<sup>10</sup> Based on the well known Hofmann clathrate compounds,<sup>11</sup> these materials are built via cyanide (CN) bridging ligands forming metallo-cyanide

planes with different linkers acting as bridges between the planes. The most representative example of this class of compounds is the family Fe(pz)[M(CN)<sub>4</sub>], with M = Ni, Pd, Pt, and pz = pyrazine.<sup>12</sup> The Fe(II) centers undergo a transition (spin crossover) from low spin to high spin, yielding a change in the magnetic, optical, dielectric, and structural properties of the material. This bistability coupled with the presence of potentially high-affinity open metal sites makes them excellent candidate materials for MOF-based gas sensing switches.<sup>4</sup>

In 2013, Arcís-Castillo et al.<sup>13</sup> studied the adsorption of SO<sub>2</sub> in the Fe(pz)[Pt(CN)<sub>4</sub>] Hofmann-type clathrate by measuring the adsorption isotherms and the x-ray diffraction patterns. The experimental results, combined with the DFT calculations established that the SO<sub>2</sub> binds strongly via chemisorption. In this work, we combine inelastic neutron scattering data with DFT calculations to further understand and clarify the SO<sub>2</sub> adsorption mechanism in the material. The most relevant signature of the binding occurs in the spectral region between 100 cm<sup>-1</sup> and 140 cm<sup>-1</sup>. The intense low energy peak at around 100 cm<sup>-1</sup> blueshifts upon adsorption, a signature that we attribute to both the hampered rotation of the pyrazine and the out-of-plane movement of the cyanide. The well defined peaks in the high-energy region of the spectra are associated with the internal vibrations of the pyrazine and are negligibly affected by the adsorbed gas. These findings are well reproduced by the computed generalized-phonon density of states and are consistent with the analysis of a strong physisorption occurring via the Pt(CN)<sub>4</sub> plane and the pyrazine molecules. This work shows that INS measurements provide a powerful tool to probe the gas adsorption mechanism in this class of materials thus allowing to unambiguously characterize the nature of the interaction when supported by DFT calculations.

## Methods

**Sample preparation.** [Fe(pz)Pt(CN)<sub>4</sub>] $\cdot$ nH<sub>2</sub>O precipitates when a solution of K<sub>2</sub>[Pt(CN)<sub>4</sub>] in H<sub>2</sub>O is added with constant stirring to a solution which contains stoichiometric amounts of pz and Fe(BF<sub>4</sub>)<sub>2</sub> $\cdot$ 6H<sub>2</sub>O in MeOH/H<sub>2</sub>O (1:1) under nitrogen at room temperature. A small amount of ascorbic acid was added to prevent the oxidation of Fe(II). After stirring for 1h, the yellow precipitate was collected by suction filtration, washed with water and methanol and dried under ambient pressure.<sup>12</sup> The sample was then heated

in a drying oven at a temperature of 100 °C.

**Gas adsorption.** The sample (722.9 mg, 1.6 mmol) was placed inside a cylindrical aluminium sample holder allowing the gas injection, connected with a capilar to a manifold gas pumping system. Temperature control was achieved using either a closed cycle cryostat (IN1-LAGRANGE) or an Orange cryostat (IN5 and PANTHER). The empty MOF was measured at 30 K. The adsorption of SO<sub>2</sub> was performed near room temperature in two injection steps until reaching a total of 1.6 mmol of SO<sub>2</sub> adsorbed, that is, one molecule of SO<sub>2</sub> per formula unit of the host. Finally, the temperature of the sample was decreased to 30 K to perform the measurements.

**IN1-LAGRANGE.** The INS experiment was performed in the indirect geometry-type spectrometer IN1-LAGRANGE<sup>14</sup> installed on the hot neutron source of the high flux reactor at the Institut Laue-Langevin (ILL) in Grenoble, France. The incident neutron energy was determined using a combination of Cu and Si monochromators for the intermediate and lower energy range respectively. Upon scattering by the sample, neutrons enter a secondary spectrometer where a beryllium filter is installed to remove higher-order harmonics in the analyser reflections. Neutrons are then reflected to a He3 gas detector at fixed final energy of 4.5 meV. This is done by using a focussing analyzer built around the vertical sample-detector axis. The scattering angle,  $\theta$ , varies from 33.7° to 69.4° and the accesible kinematical range of the instrument,  $Q$ , is defined as

$$Q^2 = k_i^2 + k_f^2 - 2k_i k_f \cos(\theta) \quad (1)$$

Where  $k_i$  and  $k_f$  are the initial and final scattering wave vectors that can be related to neutron energy by  $E = \frac{\hbar^2 k^2}{2m_n}$ ,  $m_n$  being the neutron mass. To collect the data, the incident neutron energy was scanned step-by-step by rotating the whole secondary spectrometer around the monochromator allowing the measurement of a neutron energy loss spectra. The monochromators were selected to provide the best relation between energy transfer range and resolution: we employed Cu(220), Si(311), and Si(111), respectively, for the energy transfers of [44 - 161] cm<sup>-1</sup>, [130 - 286] cm<sup>-1</sup>, and [209 - 1500] cm<sup>-1</sup>. Data were collected at 30 K for both the empty and loaded material.

**IN5.** INS data for the bare material were collected in the low energy region, i.e. < 100 cm<sup>-1</sup>, as a function of momentum transfer on the direct geometry disk chopper time-of-flight spectrometer at the ILL (Grenoble, France). The cold neutron flux from the neutron guide H16 is scattered by the sample after being turned into a pulsed monochromatic beam by a set of 6 choppers. The scattered neutrons are collected by a large cylindrical array of pixelated position-sensitive detectors (PSD) mounted inside a vacuum time-of-flight chamber, giving access to the dynamic structure factor  $S(Q, \omega)$ . Data were collected at 295 K (at low-spin state) using the standard configuration with a wavelength of 5 Å ( $E_i \approx 29.8$  cm<sup>-1</sup>) and a  $Q$  range of  $\sim 0.2 - 4.1$  Å<sup>-1</sup> for the angular detector coverage.

**PANTHER.** Complementary measurements for the low energy region were performed in the high-flux direct-geometry time-of-flight spectrometer PANTHER installed on the H12 thermal beam tube at the ILL. A double fo-

cusing pyrolytic graphite monochromator determines the incoming energy in the range 7.5 - 112 meV. Short neutron pulses produced by a slit Fermi chopper are scattered by the sample and collected by PSD. Data were collected at 10 K using an initial energy of 50 meV.

**Computational details** The DFT calculations were performed with the Quantum Espresso package<sup>15-17</sup> (v. 6.4) within the generalized gradient approximation (GGA) of Perdew, Burke and Ernzerhof (PBE)<sup>18</sup> and long-range interactions described with the semiempirical approach proposed by Grimme (PBE+D2).<sup>19,20</sup> We use the Rappe-Rabe-Kaxiras-Joannopoulos ultrasoft (rrkjus) pseudopotentials<sup>21</sup> without semicore states in valence. The convergence threshold on forces is 0.0001 Ry/Bohr and the wavefunctions and charge density cutoffs are set to 100 Ry and 1000 Ry, respectively. These are carefully chosen to obtain converged phonon frequencies. The low temperature (low spin) structure of the Hofmann clathrate was described by many authors as a disordered orientation of the pyrazines.<sup>12,22-25</sup> Recently, the present authors employed neutron diffraction data collected at D20@ILL to show an ordered configuration with the pyrazines perpendicular to each other,<sup>26</sup> a configuration that has already been observed in certain conditions.<sup>23,24,27,28</sup> To describe this perpendicular orientation a supercell with lattice parameter  $a' = \sqrt{2}a$  and  $b' = \sqrt{2}b$  was used, with  $a$  and  $b$  lattice parameters of the primitive cell. This imposes a disordered orientation (parallel in the calculations) of the pyrazines. The PBE+D2 lattice parameters of the bare MOF are i.e.  $a = 10.096$  Å,  $b = 10.097$  Å and  $c = 6.711$  Å. The Brioullin zone is sampled using 3×3×3 Monkhorst-Pack k-points grid. A revised PBE approximation for densely packed solids by Perdew et. al.<sup>29</sup> (PBEsol+D2) and the nonlocal functional rev-vdW-DF2<sup>30</sup> were used to study the effect of the functional choice on the computed density of states (see text). For rev-vdW-DF2 we employ PBE-generated pseudopotentials while for PBEsol+D2, since the convergence of the electronic structure with the rrkjus was not reached, we employed pseudopotentials from Garrity-Bennet-Rabe-Vanderbilt library (GBRV).<sup>31</sup> Wavefunctions and charge density cutoffs used for PBEsol+D2 and rev-vdW-DF2 are 70 Ry and 700 Ry. Calculations are performed using the low spin (S=0) electronic configuration.

**Generalized-phonon density of states.** The phonon frequencies were obtained by diagonalizing the dynamical matrix by employing the ph.x package in Quantum Espresso.<sup>15</sup> The harmonic interatomic force constants are computed using density functional perturbation theory.<sup>32,33</sup> The inelastic scattering data collected at IN1-LAGRANGE are compared with the computed generalized-, or neutron-weighted, phonon density of states. The  $l$ -atom contribution to the total one-phonon density of states is given by

$$g_l(\omega) = \sum_{q,j} |u_l(j, \mathbf{Q})|^2 \delta(\omega - \omega_j(\mathbf{Q})) \quad (2)$$

where  $\omega_j(\mathbf{Q})$  is the phonon frequency of the  $j$ -branch at  $\mathbf{Q}$  wavevector and  $u_l(j, \mathbf{Q})$  is the corresponding atomic displacement. Thus,  $g(\omega)d\omega$  gives the number of eigenstates in the frequency interval  $(\omega, \omega+d\omega)$ . The total generalized-phonon density of states,  $G(\omega)$ , is then defined as the phonon density of states weighted by the neutron scattering power

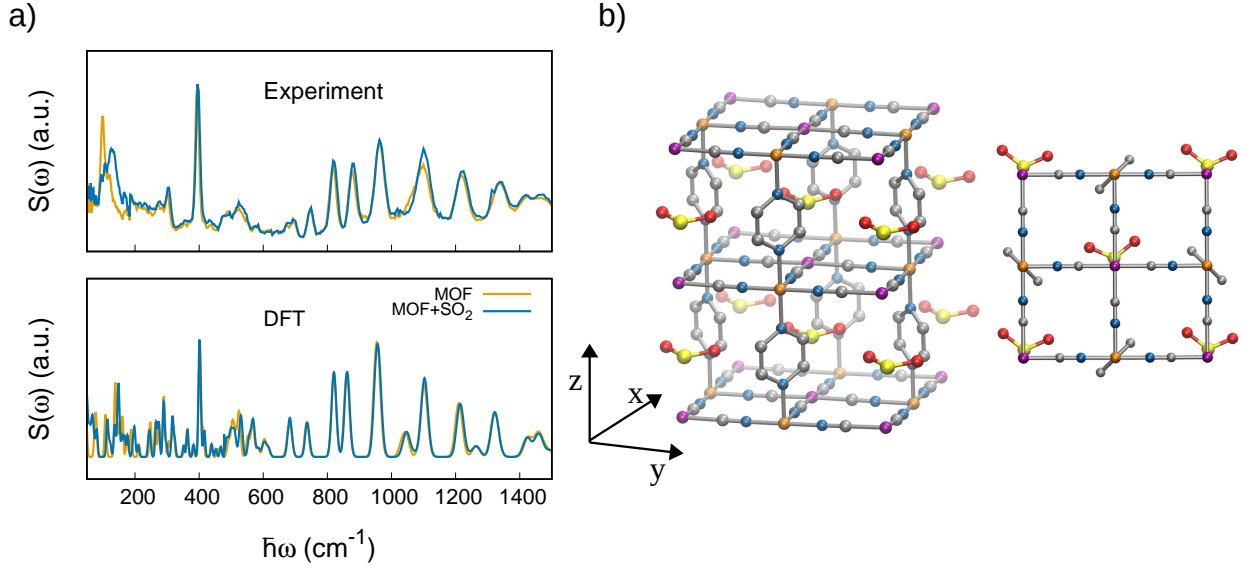


**Figure 1.** Experimental inelastic neutron scattering data,  $S(\omega)$ , collected at 30 K at IN1-LAGRANGE for the bare compound and upon  $\text{SO}_2$  uptake, upper panel (a). The  $S(\omega)$  computed using the PBE+D2 functional is reported in the lower panel (a). Side and top view illustrations of unit cell employed for the calculations containing neighboring pyrazine molecules oriented perpendicularly. Color code: purple, orange, blue, silver, red, and yellow are Pt, Fe, N, C, O, and S, respectively. H atoms are omitted for clarity.

of each atom  $l$  and it is given by

$$G(\omega) = \sum_{l=1} g_l(\omega) \frac{\sigma_l}{M_l} \quad (3)$$

where  $\sigma_l$  is the incoherent neutron scattering cross section and  $M_l$  is the mass. In the harmonic and incoherent approximation, this density of vibrational states is related to the scattering function  $S(Q, \omega)$  by the following relation<sup>34–36</sup>

$$S(Q, \omega) = e^{-2W} \frac{Q^2 \hbar}{2M\omega} < n + 1 > G(\omega) \quad (4)$$

where  $\overline{M} = \sum_l M_l / N$ ,  $n$  is the thermal-equilibrium occupation number of the vibrational state and  $< n + 1 > = \frac{\exp(\hbar\omega\beta)}{\exp(\hbar\omega\beta) - 1}$  and  $\beta = \frac{1}{k_B T}$ . We drop the vector symbol from the scattering function because for powders we measure the average over momentum transfer. The exponential term is the Debye-Waller factor for neutron attenuation by thermal motion and  $2W = \frac{Q^2 \langle u^2 \rangle}{3}$ . The average of the mean-square displacements over all the atoms is  $\langle u^2 \rangle$  and it is computed as

$$\langle u^2 \rangle = \frac{\hbar}{2MN} \sum \frac{1}{\omega_j} \coth\left(\frac{1}{2} \hbar \omega_j \beta\right) \quad (5)$$

where  $Q$  is the kinematical range of IN1-LAGRANGE (eq. 1). Because of the small  $Q$  range measured at each energy transfer, we compute phonons only at  $\Gamma$  to compare with experimental INS data, thus dropping the sum over the phonon wavevector in eq. 2. Thus eq. 4 becomes  $S(\omega)$ . This should be a fair approximation since we are measuring small  $Q$  at low energy while at high energy optical modes show small dispersion. Finally, the phonon density of states is convoluted with a Gaussian function to account for the resolution of the monochromators. We set the standard deviation of the Gaussian to  $3.0 \text{ cm}^{-1}$  for the range  $[0 - 478] \text{ cm}^{-1}$  and  $0.009\omega$  for  $[478 - 4033] \text{ cm}^{-1}$ , close to the experimental resolution of IN1-LAGRANGE.<sup>14</sup>

## Results and discussion

The INS spectra collected at IN1-LAGRANGE are shown in the upper panel of Fig. 1 for the empty and loaded MOF. The scattering function computed using eq. 4 is shown in the lower panel of Fig. 1. The full spectra including experimental errors are reported in Fig. S1. We note the need to rescale the computed  $\langle u^2 \rangle$  by a factor of 10 in order to reproduce the experimental energy decay of the spectra. This deviation may derive from the fact that only the normal modes are employed to compute eq. 5 which is a rough approximation to the full density of vibrational states, especially in the low energy region which dominates  $\langle u^2 \rangle$ .

Since the IN1 measurement is not optimized below  $100 \text{ cm}^{-1}$  (see Fig. S1), we studied this energy region for the bare material by using the time-of-flight spectrometer IN5. The data are reported in Fig. S2. These low-energy vibrational modes are associated with the vibrations of the whole lattice and with out-of-plane and in-plane vibrations of the Pt atom. Because of the difference between the computed normal modes at  $\Gamma$  and the experimental data, the assignment of the modes within this region is somehow problematic.

Between  $75$  and  $450 \text{ cm}^{-1}$  of the measured INS data, two main peaks are observed for the bare material, at  $100 \text{ cm}^{-1}$  and  $393 \text{ cm}^{-1}$ , and in between these two a less resolved region appears. Upon adsorption of  $\text{SO}_2$  the peak at  $100 \text{ cm}^{-1}$  becomes broader and shifts to higher energy, the maximum being found at  $129 \text{ cm}^{-1}$ . The remaining part of the spectrum is negligibly affected by the presence of the gas, even the strong excitation at  $393 \text{ cm}^{-1}$ . This behavior is in excellent agreement with the computational results.

The high energy region between  $700$  and  $1500 \text{ cm}^{-1}$  reveals several well defined excitations which are very well reproduced by the simulations and whose nature will be discussed later. The negligible change upon gas adsorption measured in this region is also confirmed by the calculations.

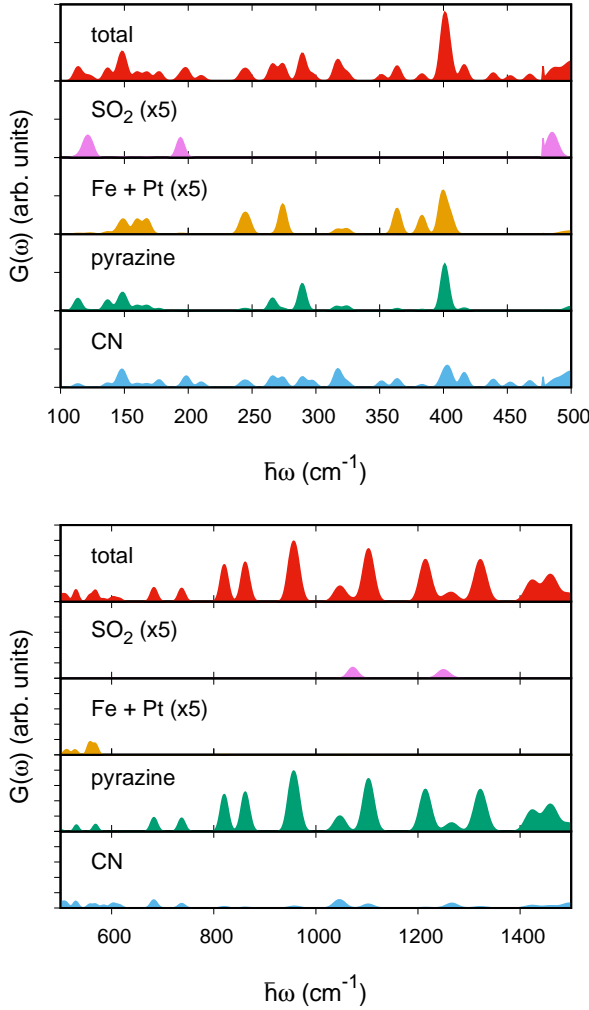


**Figure 2.** Total and partial (atom-specific) generalized phonon density of states computed for the Hofmann clathrate with adsorbed  $\text{SO}_2$  molecules. The low energy part and the high energy part are plotted separately in upper and lower panels, respectively. The partial  $g(\omega)$  of  $\text{SO}_2$  and  $\text{Pt+Fe}$  is multiplied by a factor of 5 in order to be visualized in the same scale of the  $y$  axis.

## Partial $G(\omega)$

To better analyze the nature of the measured excitations we report in Fig. 2 the partial  $G(\omega)$ , i.e. the  $g_l(\omega) \frac{\sigma_l}{M_l}$ , where  $l$  represents the different atoms or molecules in the MOF, for the Hofmann clathrate with adsorbed  $\text{SO}_2$  molecules.

In the low energy region, between 20 and  $100 \text{ cm}^{-1}$ , the  $G(\omega)$  is dominated by the vibrations of the heavy atoms, Fe and Pt, and to a minor extent by vibrations of the pyrazines and the CN groups. A few librational modes of  $\text{SO}_2$  also appear between 20 and  $120 \text{ cm}^{-1}$  (see Fig. S3). Concerning the  $\text{SO}_2$  molecule, the normal modes in the gas phase are predicted at  $484 \text{ cm}^{-1}$ ,  $1107.7 \text{ cm}^{-1}$  and  $1303.5 \text{ cm}^{-1}$  (see Fig. S3). These are respectively the scissoring (i.e. the asymmetric bending), and the symmetric and asymmetric stretches. All these modes are IR active and are found to change negligibly upon  $\text{SO}_2$  adsorption (see Fig. S3). When the molecule is adsorbed in the MOF, these are computed at

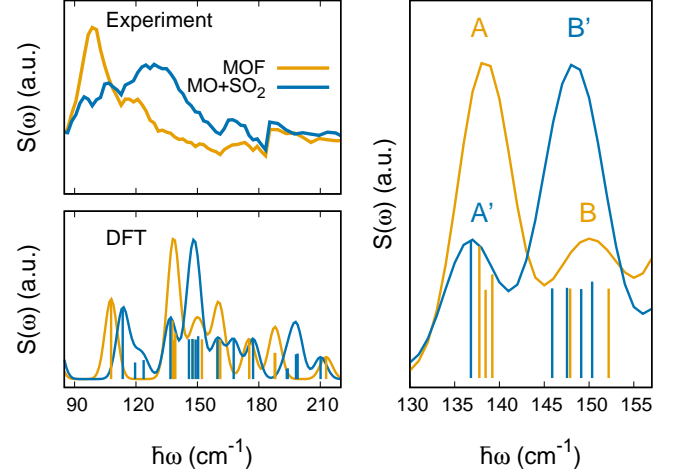


**Figure 3.** Left panels: INS spectra measured at IN1 at 30 K for the empty  $\text{Fe}(\text{pz})[\text{Pt}(\text{CN})_4]$  (orange) and after  $\text{SO}_2$  adsorption (blue) in the upper figure. The lower figure reports the computed  $S(\omega)$ . Right panel: zoom in the region  $[130 - 160] \text{ cm}^{-1}$  where the main change upon gas adsorption occurs.

$484.5$  and  $485.6 \text{ cm}^{-1}$ ,  $1042.2$  and  $1072.4 \text{ cm}^{-1}$ , and  $1248.9$  and  $1250.4 \text{ cm}^{-1}$ .

Between 100 and  $500 \text{ cm}^{-1}$ , all atoms contribute to the generalized density of states as shown in the upper panel of Fig. 2. The peaks predicted at *ca.*  $140 \text{ cm}^{-1}$  and  $400 \text{ cm}^{-1}$  have contributions mainly from the pyrazine and the CN groups as explained in more detail below, while the peak computed at  $107 \text{ cm}^{-1}$  is mainly due to a vibration of the pyrazine. At high energy, between 600 and  $1500 \text{ cm}^{-1}$ , the heavy atoms do not contribute any longer and the CN contribution is almost negligible. Here the well defined peaks are associated with vibrations of the pyrazine and their assignment is reported later. These bands exhibit a strong spectral weight due to the contribution from H atoms.

## Low-energy region

The main change upon adsorption is found in the peak at  $100 \text{ cm}^{-1}$  (see Fig. 1). The intensity of this peak decreases and a new broad feature appears centered at about  $129 \text{ cm}^{-1}$ . This result is confirmed by the INS data collected on PANTHER which are shown in Fig. S4. The peak measured on PANTHER at  $96.7 \text{ cm}^{-1}$  for the bare material should correspond to the intense band measured at  $94.4 \text{ cm}^{-1}$  on IN1 (see Fig. S2). In this region, the most intense bands predicted by the calculations for the bare material appear at  $107.9 \text{ cm}^{-1}$  and at  $139 \text{ cm}^{-1}$ , as shown in Fig. 3. The first one corresponds to the rotation of the pyrazine around the  $z$  axis, in agreement with calculations by Hochdörffer et al.<sup>37</sup> on a 3D molecular cluster composed of several repetitions of the clathrate unit cell. The second band includes 3 vibrational modes at energies  $137.8$ ,  $138.5$ , and  $139.2 \text{ cm}^{-1}$ . We name this second intense peak A in Fig. 3 to assist the analysis. The first peak at  $137.8 \text{ cm}^{-1}$  is a collective mode involving a movement of the CN group with contributions from in-plane and out-of-plane, together with a rotation of the pyrazine around the  $z$  axis. The second at  $138.5 \text{ cm}^{-1}$

involves a rigid out-of-plane twisting of the  $\text{Fe}(\text{CN})_4\text{N}_2$  octahedra yielding a rigid twisting of the pyrazine about the  $y$  axis. This vibrational mode corresponds to the one computed at  $140\text{ cm}^{-1}$  in ref. 37. The vibration at  $139.2\text{ cm}^{-1}$  involves a large out-of-plane vibration of the cyanide together with a small libration of the pyrazine. The change in the eigenvectors is illustrated in Fig. S5. Upon gas uptake, the vibration at  $107.9\text{ cm}^{-1}$  blueshifts to  $113.5\text{ cm}^{-1}$  possibly due to steric hindrance by the  $\text{SO}_2$  molecule and it becomes coupled with a libration of  $\text{SO}_2$ . Two new modes consisting of pure  $\text{SO}_2$  librations appear at  $119.5$  and  $123.7\text{ cm}^{-1}$ . Under peak A, the first mode barely changes (i.e.  $137.8 \rightarrow 136.8\text{ cm}^{-1}$ ) while the second and third blueshift by 9 and  $10\text{ cm}^{-1}$ , respectively (i.e.  $138.5 \rightarrow 147.5\text{ cm}^{-1}$ , and  $139.2 \rightarrow 149.1\text{ cm}^{-1}$ ). The Pt atom does not participate in these vibrations for the bare MOF, but upon gas adsorption the heavy atom contributes to the out-of-plane bending of the cyanide for the mode at  $149.1\text{ cm}^{-1}$ . For the bare MOF the peak named B in Fig. 3 includes two vibrations at  $147.9\text{ cm}^{-1}$  and  $152.2\text{ cm}^{-1}$ . These correspond to an in-plane movement of the Pt atoms together with a rigid in-plane displacement of the pyrazines. Upon adsorption these slightly redshift to  $145.9\text{ cm}^{-1}$  and  $150.4\text{ cm}^{-1}$ , respectively. All of the vibrations found in peaks A' and B' exhibit a negligible contribution from  $\text{SO}_2$ .

Because the scattering cross section of hydrogen,  $\sigma_H = 82.0$  barn, is significantly larger than any other atom (Fe and Pt for example have 11.62 and 11.71 barn, respectively), the gas adsorption mechanism is here probed mainly through changes in the riding modes of H, i.e. those modes that involve vibrations of the hydrogens.<sup>38</sup> As described above, in this region, the vibrations that imply the rotation of the pyrazine around the  $z$  axis and the cyanide out-of-plane movement shift to higher energy while those exhibiting in-plane bendings of cyanides show a negligible shift. We attribute the blueshift of this peak predicted at *ca.*  $139\text{ cm}^{-1}$  to an increase of the cyanide out-of-plane bending force constant due to steric hindrance, similarly to the hindered rotation of the pyrazine predicted at  $107\text{ cm}^{-1}$ .

While the assignment of the experimental peak at  $400\text{ cm}^{-1}$  can be performed without ambiguity based on the good agreement with the calculations, the intense band at  $100\text{ cm}^{-1}$  may be assigned either to the group of bands predicted at  $137.8$ ,  $138.5$ , and  $139.2\text{ cm}^{-1}$ , or to these bands together with the peak at  $107\text{ cm}^{-1}$ . The intensity of the well defined peak predicted by DFT at *ca.*  $400\text{ cm}^{-1}$  includes two normal modes at  $403.5$  and  $405\text{ cm}^{-1}$  which are associated with the torsion of the pyrazine. It undergoes a blueshift upon gas adsorption of  $0.8\text{ cm}^{-1}$  and a redshift of  $2.06\text{ cm}^{-1}$  for the duplicated mode. The predicted negligible change in the energy of this vibration by the DFT calculations is in agreement with the small change found experimentally (see Fig. 1).

## The $\text{SO}_2$ binding mechanism

The molecular orbital interaction of  $\text{SO}_2$  with this MOF was previously studied by Arcís-Castillo *et al.*<sup>13</sup> using DFT calculations and it was reported before by many authors for other metal complexes.<sup>39–42</sup> The results of our calculations agree with those of Arcís-Castillo *et al.* except for the interpretation: we do not identify the mixing between the hybridized Pt  $d_{z^2}$ - $p_z$  orbital<sup>43</sup> and the  $\pi^*$  LUMO (lowest unoccupied molecular orbital) of the  $\text{SO}_2$  as a  $\pi$ -backbonding

because of the absence of  $\pi$  symmetry in this interaction.<sup>43</sup> Below we discuss in more detail the molecular orbital interaction between  $\text{SO}_2$  and the metal center.

When  $\text{SO}_2$  binds on top of a metal with square planar coordination, a strong electron donor interaction may be achieved when the  $\sigma$  HOMO (highest occupied molecular orbital) of the molecule can donate electron density to the empty  $d_{z^2}$  of the metal. In this case the expected binding configuration is the  $\eta^1$ -planar<sup>40</sup> as illustrated and discussed in ref. 13. Because for a  $d^8$  electron count the  $d_{z^2}$  is doubly occupied, the molecule can act only as an electron acceptor.<sup>42</sup> Since the  $d_{z^2}$  is fully occupied, the molecule orients in such a way to decrease the antibonding  $\sigma$ -type of interaction between the HOMO of the molecule and the Pt  $d_{z^2}$ , thus adopting an  $\eta^1$ -pyramidal configuration<sup>40</sup> with the angle between the Pt and the molecular plane of the  $\text{SO}_2$  being  $\theta=101.2^\circ$  (PBE+D2). In this bent configuration, the LUMO of the molecule interacts with a polarized molecular orbital of Pt (see Fig. S6) which is a hybridized Pt  $d_{z^2}$ - $p_z$  orbital, the polarized character resulting from the addition (bigger lobe) and cancellation (smaller lobe) of the two  $d_{z^2}$  and  $p_z$  amplitudes.<sup>43</sup> Such polarized character reduces the antibonding interaction. Possibly because of the bent configuration that would reduce the  $\pi$  type overlap, the interaction of the  $\pi^*$  LUMO does not occur with the  $d_{xz}$  or  $d_{yz}$  orbitals of Pt.

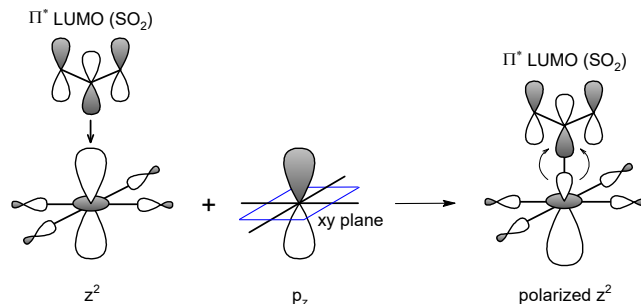


**Figure 4.** Molecular orbital picture of the interaction between the  $\text{SO}_2$  LUMO and the polarized hybridized  $d_{z^2}$ - $p_z$  orbital of Pt. Because this unoccupied electronic state involves a contribution from the Pt- $d_{z^2}$  that is fully occupied in the bare material, such interaction results in a metal  $\rightarrow$  molecule charge transfer.

On the basis of the discussed binding mechanism,  $\text{SO}_2$  is thus expected to act as an electron acceptor. The Bader charge analysis performed in this work using PAW pseudopotentials reveals a rather small charge transfer from the MOF to the molecule of 0.12 electrons, suggesting that other effects possibly related to the MOF skeleton may contribute to the large value of the computed binding energy per  $\text{SO}_2$  molecule, i.e.  $0.769\text{ eV}$  (with PBE+D2). This value decreases to  $0.210\text{ eV}$  upon full geometrical optimization after the D2 correction is removed. We note the stronger binding computed by Arcís-Castillo *et al.*<sup>13</sup> using PBEsol+D2. They predict a binding energy of  $0.977\text{ eV}$ , in agreement with the value that we compute when using the same functional, i.e.  $0.953\text{ eV}$ . To corroborate this, we computed the binding energy of  $\text{SO}_2$  only with the two  $\text{Fe}[\text{Pt}(\text{CN})_4]$  planes, respectively below and above the molecule, by fixing all the atomic coordinates to the relaxed geometry in the MOF. The lattice parameters in the plane are set to those of the MOF while we imposed a large  $c$  cell parameter in order to reduce inter-



action between the images along  $z$ . The binding energy is 0.274 eV. This large energy difference between the two cases points to a binding mechanism originating from a combined charge transfer mechanism with the  $\text{Fe}[\text{Pt}(\text{CN})_4]$  planes via the  $\text{SO}_2$ -Pt interaction, together with a strong interaction with the rest of the MOF skeleton.

An efficient way to improve the treatment of electronic correlations in DFT is to adopt the DFT+ $U$  approach where the Hubbard  $U$  correction is computed in terms of some localized Hubbard states. We employ the simplified rotationally invariant formulation<sup>44</sup> as implemented in Quantum Espresso. To study how the change in hybridization<sup>45</sup> of the localized  $d$  states of Pt upon  $U$  correction affects the binding mechanism,<sup>46</sup> we employ ortho-atomic projectors to compute self-consistently the linear-response  $U$  parameters associated to the  $d$  states of Pt (5.2 eV) and Fe (7.5 eV), using density functional perturbation theory.<sup>47</sup> By setting the atomic coordinates to the optimized PBE+D2, we compute a DFT+ $U$  binding energy of 0.617 eV. When the geometry is allowed to fully relax using PBE+D2+ $U$ , we predict a  $\text{SO}_2$  binding energy of 0.680 eV. The full optimization with Hubbard  $U$  gives a significantly different  $\text{SO}_2$  binding geometry with respect to PBE+D2 case. Tab. 1 reports the binding energy, bond distance and bond angles computed with the different schemes. The S-Pt bond distance changes from 2.933 Å (PBE+D2) to 3.460 Å (PBE+D2+ $U$ ) and the Pt-S-O angle from 101.2° to 95.0°. The  $\text{SO}_2$  bond angle, O-S-O, slightly increases upon  $U$  correction (see Tab. 1). The projected density of states shown in Fig. S7 reveals a lower contribution from the polarized Pt atoms (see Fig. 4) to the states associated with the LUMO of the molecule, consistent with a reduced charge transfer mechanism and larger  $\text{SO}_2$  bending angle. We note that the reported experimental Pt-S bond distance at 120 K is 2.585 Å,<sup>13</sup> significantly shorter than the PBE+D2+ $U$  one. This elongation of bond lengths upon  $U$  correction has already been reported and discussed by some of us<sup>45</sup> and is the reason behind the choice of the PBE+D2 geometry in the calculation of the vibrational modes. Because of this bond elongation and because the use of DFT+ $U$  may lead to a bias when computing total energy differences,<sup>48</sup> we also report the binding energy computed using a DFT+ $U$  density-corrected approach by employing the DFT+D2 geometry. This consists in using the PBE+D2 total energy evaluated on the PBE+D2+ $U$  electronic density, an approach that we have named PBE+D2[U]. We compute a binding energy of 0.730 eV.

This result together with the above analysis of the binding mechanism indicate that the  $\text{SO}_2$  adsorption occurs via a physisorption mechanism, the high value of the computed binding energy arising from a combination of stabilizing electrostatic and van der Waals forces.

## High-energy region

The high energy region, which is dominated by the vibrations of the pyrazine, negligibly changes upon gas adsorption. We have computed the  $G(\omega)$  of the pyrazine in gas phase and we report the comparison with the partial  $G(\omega)$  of the pyrazine in the compound in Fig. S8. The complexation of the pyrazine in the MOF slightly modifies the position of the vibrational modes with respect to the gas phase. A comparison and a brief description of the modes is reported in Table 2. These were studied by various authors by employing IR and Raman spectroscopies<sup>49–55</sup> and INS.<sup>56</sup> Three different spectral regions can be identified for the free and complexed pyrazine: (i) in-plane CH bendings and ring stretching motions in [990 - 1600]  $\text{cm}^{-1}$ , (ii) intense bands associated with the CH out-of-plane deformation vibrations at [700 - 990]  $\text{cm}^{-1}$ , and (iii) CH stretching near 3000  $\text{cm}^{-1}$ . The vibrations with predominant CC and CN character can be further divided into C-C and C-N stretching modes at 1058 - 1551  $\text{cm}^{-1}$ , in-plane bending modes at 580  $\text{cm}^{-1}$  and 690  $\text{cm}^{-1}$  and out-of-plane bending in the region 750 - 990  $\text{cm}^{-1}$  and below 500  $\text{cm}^{-1}$  like 413  $\text{cm}^{-1}$  and 312  $\text{cm}^{-1}$ . The characteristic breathing mode of the pyrazine appears at 1009  $\text{cm}^{-1}$ . As a general trend the complexation with Fe(II) blueshifts the vibrational modes of the free pyrazine. This effect is possibly driven by an electron-acceptor effect of the pyrazine from the occupied  $d$  orbitals of the metal<sup>57</sup> that increases the  $\pi$  cloud of the ring: thus the stronger double bond character increases the vibrational frequencies.<sup>58</sup> We note that the CH out-of-plane bending mode at 913  $\text{cm}^{-1}$  undergoes the opposite effect and redshifts to *ca.* 859  $\text{cm}^{-1}$  thus appearing in the gap between [760 - 910]  $\text{cm}^{-1}$  of the free pyrazine (see Fig. 2).

## Choice of the supercell

Several authors have reported a specific long range ordering of the pyrazine ligands within these materials as a consequence of gas adsorption.<sup>23,24,28</sup> In the absence of diffraction data, we assessed the ordering of the pyrazine upon  $\text{SO}_2$  adsorption using DFT calculations. We performed two supercell calculations where we impose that the pyrazines are oriented either perpendicularly with neighboring ones or parallel. We find negligible energy differences between these two configurations when the material is loaded with one  $\text{SO}_2$  molecule per Pt atom. We recall that for the bare material such energy difference becomes 39 meV/f.u.<sup>26</sup> The comparison between the corresponding generalized phonon density of states and that of the bare material, however, shows that the configuration with all pyrazines oriented parallel with one another results in a predicted  $G(\omega)$  exhibiting some deviations from the bare material that are not observed ex-

**Table 1.** Comparison of the binding energy, bond distance and bond angles computed using the different functionals. The PBE+D2 computed  $\text{SO}_2$  bond angle for the isolated molecule is 119.4°.

	$E_{\text{bind}}(\text{eV})$	$d(\text{S-Pt}) (\text{\AA})$	$\angle(\text{Pt-S-O}) (^\circ)$	$\angle(\text{O-S-O}) (^\circ)$
PBE	0.239	2.895	102.4	116.8
PBE+D2	0.769	2.933	101.2	117.2
PBE+D2+ $U$	0.683	3.470	95.2	118.2
PBE+D2[U]	0.730	2.933	101.2	117.2
PBEsol+D2	0.911	2.786	102.1	116.8

perimentally. The comparison between the empty (pyrazine perpendicular) and the loaded material is reported in Fig. 5.

The configuration with parallel pyrazines upon  $\text{SO}_2$  adsorption results in a noticeable change in the intense peak at  $400 \text{ cm}^{-1}$  with respect to the bare material, a feature that is not observed in the experiment. Similarly, the high energy features between  $800$  and  $1000 \text{ cm}^{-1}$  redshift in the configuration with parallel pyrazines, suggesting that the INS data may correspond to a configuration with pyrazines oriented perpendicularly with each other both before and after gas adsorption.

We tested a few functional choices on the computed  $G(\omega)$  for the bare material. For this we employed the primitive cell (thus imposing parallel pyrazines) and the exchange and correlation functionals PBEsol+D2, rev-vdW-DF2, and PBE+D2. The three functionals give very similar results. At high energy, the spectra negligibly depend on the specific choice while at low energy, as expected, they are more strongly affected by the approximation to the exchange and correlation energy,<sup>59</sup> as shown in Fig. S9. Specifically, we see a tendency to predict higher frequencies in this region using PBEsol+D2, as compared with PBE+D2, consistent with shorter bond distances and smaller lattice parameters.

## Conclusion

The  $\text{SO}_2$  adsorption mechanism in the  $\text{Fe}(\text{pz})[\text{Pt}(\text{CN})_4]$  Hofmann clathrate is here probed by combining inelastic neutron scattering experiments and DFT calculations. The most noticeable change upon adsorption is the blueshift of the peak measured at *ca.*  $100 \text{ cm}^{-1}$  which we attribute to

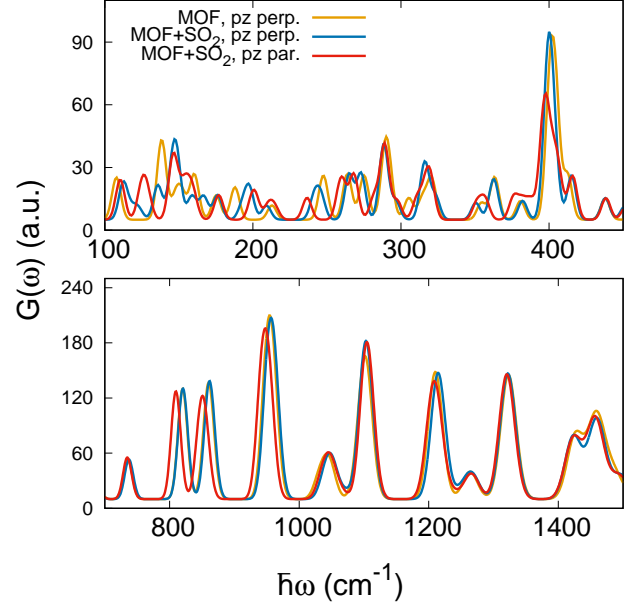


**Figure 5.** Total  $G(\omega)$  in the low (upper panel) and high (lower panel) computed for the bare material with perpendicularly oriented pyrazines (yellow), and for the material loaded with one  $\text{SO}_2$  per Pt site computed by employing perpendicular (blue) or parallel (red) pyrazines.

**Table 2.** Energy position of the peaks measured from the INS data for the bare MOF, the calculated values in the bare MOF and for pyrazine in gas phase, and their assignment. We could not find a correspondence for the modes whose energy is re

Experiment (INS)	DFT - pz@MOF				DFT - gas phase pz		Assignment
-	3168	3167	3165	3164	3059	3067	CH stretching
-	3155	3153	3152	3150	3088	3092	CH stretching
1601	1597	1596			1551		CH in-plane bending, CC stretch
1482	1487	1486			1525		CN and CC stretch
1472	1459	1458			1472		CH in-plane bending, CN stretch
1430	1426.8	1426.3			1389		CH in-plane bending, CN and CC stretch
1338	1323	1322			1324		CH in-plane bending, CN stretch
1220	1263.9	1263.6			1225		CN and CC stretch
1220	1211	1208			1209		CH in-plane bending, CN and CC stretch
1105	1105	1104			1058		CH in-plane bending, CN and CC stretch
1105	1099	1093			1128		CH in-plane bending, CN stretch
1105	1047	1045			996		CN in-plane bending
1105	1032	1031			1009		Breathing mode
959	960	959			967		CH out-of-plane bending, CNC twisting
959	949.9	949.4			959		CH out-of-plane bending, CNC wagging
876	862	857			913		CH out-of-plane bending, CNC twisting
817	820	819			725		CH out-of-plane bending, CNC wagging
749	735.6	735.5			757		CH out-of-plane bending, CNC wagging
696	687	685			690		CNC in-plane bending
674	680	676			580		CNC in-plane bending
394	403	404			312		CH out-of-plane bending, CNC twisting
-	566	525			413		CH out-of-plane bending, CNC wagging



an increase of the cyanide out-of-plane bending force constant due to steric hindrance and to the hindered rotation of the pyrazine around the  $z$  axis. The experimental observations are consistent with an adsorption mechanism being a combined charge transfer, electrostatic and dispersion interactions, as predicted by the DFT calculations. The high-energy peaks which are associated with the internal vibrations of the pyrazine molecule are negligibly affected by the presence of the physisorbed gas molecule. Based on these findings we expect a different signature of the adsorption of different molecules such as CO or CO<sub>2</sub> on the INS data and are confident that the present joint computational and experimental scheme will allow to characterize the gas interaction mechanism in these family of materials.

**Acknowledgement** This work benefited from the support of the project ANR-15-CE06-0003-01 funded by the French National Agency for Research. Calculations were performed using resources granted by GENCI under the CINES and TGCC grant numbers A0020907211 and A0110907211. Additionally, the froggy and Dahu platform of the CIMENT infrastructure, which is supported by the Rhone-Alpes region (GRANT CPER07\_13 CIRA) and the Equip@Meso project, was employed for the calculations. We thank the ILL for the PhD contract of A.F.B. and for the beamtime allocation under experiment numbers 7-02-108, 7-05-513, and 7-05-430 (doi.ill.fr/10.5291/ILL-DATA.7-05-430). J.A.R. acknowledges resources from Grant PID2019-106147GB-I00 funded by MCIN/AEI/10.13039/501100011033.

## References

- (1) Li, J.-R.; Kuppler, R. J.; Zhou, H.-C. Selective gas adsorption and separation in metal-organic frameworks. *Chem. Soc. Rev.* **2009**, *38*, 1477–1504.
- (2) Yang, C.-T.; Kshirsagar, A. R.; Eddin, A. C.; Lin, L.-C.; Poloni, R. Tuning Gas Adsorption by Metal Node Blocking in Photoresponsive Metal-Organic Frameworks. *Chem. Eur. J.* **2018**, *24*, 15167–15172.
- (3) He, L.; Liu, Y.; Liu, J.; Xiong, Y.; Zheng, J.; Liu, Y.; Tang, Z. Core-Shell Noble-Metal@Metal-Organic-Framework Nanoparticles with Highly Selective Sensing Property. *Angew. Chem. Int. Ed.* **2013**, *52*, 3741–3745.
- (4) Li, H.-Y.; Zhao, S.-N.; Zang, S.-Q.; Li, J. Functional metal-organic frameworks as effective sensors of gases and volatile compounds. *Chem. Soc. Rev.* **2020**, *49*, 6364–6401.
- (5) Gamonal, A.; Sun, C.; Mariano, A. L.; Fernandez-Bartolome, E.; Guerrero-SanVicente, E.; Vlasisavljevic, B.; Castells-Gil, J.; Marti-Gastaldo, C.; Poloni, R.; Wanemacher, R.; Cabanillas-Gonzalez, J.; Costa, J. S. Divergent Adsorption-Dependent Luminescence of Amino-Functionalized Lanthanide Metal-Organic Frameworks for Highly Sensitive NO<sub>2</sub> Sensors. *J. Phys. Chem. Lett.* **2020**, *11*, 3362–3368.
- (6) Muñoz, M. C.; Real, J. A. Thermo-, piezo-, photo- and chemoswitchable spin crossover iron(II)-metallocyanate based coordination polymers. *Coordination Chemistry Reviews* **2011**, *255*, 2068–2093, Special Issue: 39th International Conference on Coordination Chemistry.
- (7) Ni, Z.-P.; Liu, J.-L.; Hoque, M. N.; Liu, W.; Li, J.-Y.; Chen, Y.-C.; Tong, M.-L. Recent advances in guest effects on spin-crossover behavior in Hofmann-type metal-organic frameworks. *Coordination Chemistry Reviews* **2017**, *335*, 28–43.
- (8) Ding, M.; Flaig, R. W.; Jiang, H.-L.; Yaghi, O. M. Carbon capture and conversion using metal-organic frameworks and MOF-based materials. *Chem. Soc. Rev.* **2019**, *48*, 2783–2828.
- (9) Guo, Z.; Wu, H.; Srinivas, G.; Zhou, Y.; Xiang, S.; Chen, Z.; Yang, Y.; Zhou, W.; O’Keeffe, M.; Chen, B. A Metal-Organic Framework with Optimized Open Metal Sites and Pore Spaces for High Methane Storage at Room Temperature. *Angew. Chem. Int. Ed.* **2011**, *50*, 3178–3181.
- (10) Reed, D. A.; Keitz, B. K.; Oktawiec, J.; Mason, J. A.; Runčevski, T.; Xiao, D. J.; Darago, L. E.; Crocellà, V.; Bordiga, S.; Long, J. R. A spin transition mechanism for cooperative adsorption in metal-organic frameworks. *Nature* **2017**, *550*, 96–100.
- (11) Hofmann, K. A.; Küspert, F. Verbindungen von Kohlenwasserstoffen mit Metallsalzen. *Zeitschrift für anorganische Chemie* **1897**, *15*, 204–207.
- (12) Niel, V.; Martinez-Agudo, J. M.; Muñoz, M. C.; Gaspar, A.; Real, J. Cooperative Spin Crossover Behavior in Cyanide-Bridged Fe(II)-M(II) Bimetallic 3D Hofmann-like Networks (M = Ni, Pd and Pt). *Inorg. Chem.* **2001**, *40*, 3838–3839.
- (13) Arcís-Castillo, Z.; Muñoz-Lara, F.; Muñoz, M.; Aravena, D.; Gaspar, A.; Sánchez-Royo, J.; Ruiz, E.; Ohba, M.; Matsuda, R.; Kitagawa, S.; Real, J. Reversible Chemisorption of Sulfur Dioxide in a Spin Crossover Porous Coordination Polymer. *Inorg. Chem.* **2013**, 12777–12783.
- (14) Ivanov, A.; Jimenez-Ruiz, M.; Kulda, J. IN1-LAGRANGE – the new ILL instrument to explore vibration dynamics of complex materials. *Journal of Physics: Conference Series* **2014**, *554*, 012001.
- (15) Giannozzi, P. et al. QUANTUM ESPRESSO: a modular and open-source software project for quantum simulations of materials. *J. Phys. Condens. Matter* **2009**, *21*, 395502.
- (16) Giannozzi, P. et al. Advanced capabilities for materials modelling with Quantum ESPRESSO. *J. Phys. Condens. Matter* **2017**, *29*, 465901.
- (17) Giannozzi, P.; Barone, O.; Bonfà, P.; Brunato, D.; Car, R.; Carnimeo, I.; Carvazzoni, C.; de Gironcoli, S.; Delugas, P.; Ruffino, F. F.; Ferreti, A.; Mazari, N.; Timrov, I.; Urru, A.; Baroni, S. QUANTUM ESPRESSO toward the exascale. *Journal of Chemical Physics* **2020**, *152*, 154105–1 – 154105–11.
- (18) Perdew, J. P.; Ernzerhof, M.; Burke, K. Rationale for mixing exact exchange with density functional approximations. *J. Chem. Phys.* **1996**, *105*, 9982–9985.
- (19) Grimme, S. Semiempirical GGA-type density functional constructed with a long-range dispersion correction. *J. Comput. Chem.* **2006**, *27*, 1787–1799.
- (20) Grimme, S.; Hansen, A.; Brandenburg, J. G.; Bannwarth, C. Dispersion-Corrected Mean-Field Electronic Structure Methods. *Chem. Rev.* **2016**, *116*, 5105–5154, PMID: 27077966.
- (21) Rappe, A. M.; Rabe, K. M.; Kaxiras, E.; Joannopoulos, J. D. Optimized pseudopotentials. *Phys. Rev. B* **1990**, *41*, 1227–1230.
- (22) Rodríguez-Velamazán, J. A.; González, M. A.; Real, J. A.; Castro, M.; Muñoz, M. C.; Gaspar, A. B.; Ohtani, R.; Ohba, M.; Yoneda, K.; Hijikata, Y.; Yanai, N.; Mizuno, M.; Ando, H.; Kitagawa, S. A Switchable Molecular Rotator: Neutron Spectroscopy Study on a Polymeric Spin-Crossover Compound. *J. Am. Chem. Soc.* **2012**, *134*, 5083–5089, PMID: 22364147.
- (23) Southon, P. D.; Liu, L.; Fellows, E. A.; Price, D. J.; Halder, G. J.; Chapman, K. W.; Moubarak, B.; Murray, K. S.; Létard, J.-F.; Kepert, C. J. Dynamic Interplay between Spin-Crossover and Host-Guest Function in a Nanoporous Metal-Organic Framework Material. *J. Am. Chem. Soc.* **2009**, *131*, 10998–11009.
- (24) Ohba, M.; Yoneda, K.; Agustí, G.; Muñoz, M.; Gaspar, A.; Real, J.; Yamasaki, M.; Ando, H.; Nakao, Y.; Sakaki, S.; Kitagawa, S. Bidirectional Chemo-Switching of Spin State in a Microporous Framework. *Angew. Chem. Int. Ed.* **2009**, *48*, 4767–4771.
- (25) Cobo, S.; Ostrovskii, D.; Bonhommeau, S.; Vendier, L.; Molnár, G.; Salmon, L.; Tanaka, K.; Bousseksou, A. Single-Laser-Shot-Induced Complete Bidirectional Spin Transition at Room Temperature in Single Crystals of (FeII(pyrazine))(Pt(CN)<sub>4</sub>). *J. Am. Chem. Soc.* **2008**, *130*, 9019–9024.
- (26) Fernandez-Blanco, A.; Mariano, L. A.; Piñeiro-Lopez, L.; Real, J.; Sanchez-Costa, J.; Poloni, R.; Rodríguez-Velamazán, J. A. Hidden ordered structure in the archetypical Fe(pyrazine)[Pt(CN)<sub>4</sub>] spin-crossover porous coordination compound. *in preparation*
- (27) Rodríguez-Hernández, J.; Lemus-Santana, A.; Ortiz-López, J.; Jiménez-Sandoval, S.; Reguera, E. Low temperature structural transformation in T[Ni(CN)<sub>4</sub>]-xpyz with x=1,2; T=Mn,Co,Ni,Zn,Cd; pyz=pyrazine. *Journal of Solid State Chemistry* **2010**, *183*, 105–113.
- (28) Aravena, D.; Castillo, Z. A.; Muñoz, M. C.; Gaspar, A. B.; Yoneda, K.; Ohtani, R.; Mishima, A.; Kitagawa, S.; Ohba, M.; Real, J. A.; Ruiz, E. Guest Modulation of Spin-Crossover Transition Temperature in a Porous Iron(II) Metal-Organic Framework: Experimental and Periodic DFT Studies. *Chemistry – A European Journal* **2014**, *20*, 12864–12873.
- (29) Perdew, J. P.; Ruzsinszky, A.; Csonka, G. I.; Vydrov, O. A.; Scuseria, G. E.; Constantin, L. A.; Zhou, X.; Burke, K. Restoring the Density-Gradient Expansion for Exchange in Solids and Surfaces. *Phys. Rev. Lett.* **2008**, *100*, 136406.
- (30) Hamada, I. van der Waals density functional made accurate. *Phys. Rev. B* **2014**, *89*, 121103.
- (31) Garrity, K. F.; Bennett, J. W.; Rabe, K. M.; Vanderbilt, D. Pseudopotentials for high-throughput DFT calculations. *Comput. Mater. Sci.* **2014**, *81*, 446–452.
- (32) Baroni, S.; de Gironcoli, S.; Dal Corso, A.; Giannozzi, P. Phonons and related crystal properties from density-functional perturbation theory. *Rev. Mod. Phys.* **2001**, *73*, 515–562.
- (33) Gonze, X.; Lee, C. Dynamical matrices, Born effective charges, dielectric permittivity tensors, and interatomic force constants from density-functional perturbation theory. *Phys. Rev. B* **1997**, *55*, 10355–10368.
- (34) Squires, G. *Introduction to the Theory of Thermal Neutron Scattering*; Dover books on physics; Dover Publications, 1996.
- (35) Price, D.; Carpenter, J. Scattering function of vitreous silica. *J. Non Cryst. Solids* **1987**, *92*, 153–174.
- (36) Taraskin, S. N.; Elliott, S. R. Connection between the true vi-

- brational density of states and that derived from inelastic neutron scattering. *Phys. Rev. B* **1997**, *55*, 117–123.
- (37) Hochdörffer, T.; Chumakov, A. I.; Wille, H.-C.; Schünemann, V.; Wolny, J. A. Vibrational properties and cooperativity of the 3D spin crossover network [Fe(pyrazine)][Pt(CN)<sub>4</sub>]. *Dalton Trans.* **2019**, *48*, 15625–15634.
  - (38) Mitchell, P.; Parker, S.; Ramirez-Cuesta, A.; Tomkinson, J. *Series on Neutron Techniques and Applications*.
  - (39) Muir, K. W.; Ibers, J. A. Structure of chlorocarbonyl(sulfur dioxide)bis(triphenylphosphine)rhodium, RhCl(CO)(SO<sub>2</sub>)(P(C<sub>6</sub>H<sub>5</sub>)<sub>3</sub>)<sub>2</sub>. *Inorg. Chem.* **1969**, *8*, 1921–1928.
  - (40) Ryan, R.; Kubas, G.; Moody, D.; Eller, P. Structure and Bonding of Transition Metal-Sulfur Dioxide Complexes. *Inorg. Chem.* **1981**, 47–100.
  - (41) Mingos, D. Sulphur Dioxide Complexes of the Platinum Metals. *Transition Met. Chem.* **1978**, 1–15.
  - (42) Mingos, D. Ambivalent Lewis Acid/Bases with Symmetry Signatures and Isolobal Analogies. *Struct. Bond.* **2014**, 1–52.
  - (43) Jean, Y. *Molecular orbitals of transition metal complexes*; Oxford University Press, 2005; pp 19,55–56.
  - (44) Dudarev, S. L.; Botton, G. A.; Savrasov, S. Y.; Humphreys, C. J.; Sutton, A. P. Electron-energy-loss spectra and the structural stability of nickel oxide: An LSDA+U study. *Phys. Rev. B* **1998**, *57*, 1505–1509.
  - (45) Mariano, L. A.; Vlasisavljevich, B.; Poloni, R. Improved Spin-State Energy Differences of Fe(II) Molecular and Crystalline Complexes via the Hubbard U-Corrected Density. *Journal of Chemical Theory and Computation* **2021**, *17*, 2807–2816, PMID: 33831303.
  - (46) Mann, G. W.; Lee, K.; Cococcioni, M.; Smit, B.; Neaton, J. B. First-principles Hubbard U approach for small molecule binding in metal-organic frameworks. *The Journal of Chemical Physics* **2016**, *144*, 174104.
  - (47) Timrov, I.; Marzari, N.; Cococcioni, M. Hubbard parameters from density-functional perturbation theory. *Phys. Rev. B* **2018**, *98*, 085127.
  - (48) Mariano, L. A.; Vlasisavljevich, B.; Poloni, R. Biased Spin-State Energetics of Fe(II) Molecular Complexes within Density-Functional Theory and the Linear-Response Hubbard U Correction. *J. Chem. Theory Comput.* **2020**, *16*, 6755–6762, PMID: 33108722.
  - (49) Ito, M.; Shimada, R.; Kuraishi, T.; Mizushima, W. Vibrational Spectra of Diazines. *J. Chem. Phys.* **1956**, *25*, 597–598.
  - (50) Lord, R.; Marston, A.; Miller, F. A. Infra-red and Raman spectra of the diazines. *Spectrochimica Acta* **1957**, *9*, 113–125.
  - (51) Katritzky, A. R. The infrared spectra of heteroaromatic compounds. *Q. Rev. Chem. Soc.* **1959**, *13*, 353–373.
  - (52) Califano, S.; Adembri, G.; Sbrana, G. Vapour and crystal spectra in polarized light of pyrazine-d<sub>0</sub>, cis pyrazine-d<sub>2</sub> and pyrazine-d<sub>4</sub>. *Spectrochimica Acta* **1964**, *20*, 385–396.
  - (53) Simmons, J.; Innes, K.; Begun, G. Infrared and Raman Spectra of Pyrazine-h<sub>4</sub> and -d<sub>4</sub>. *J. Mol. Spectrosc.* **1964**, 190 – 197.
  - (54) Arenas, J. F.; Lopez-Navarrete, J. T.; Otero, J. C.; Marcos, J. I.; Cardenete, A. Vibrational spectra of [1H<sub>4</sub>]pyrazine and [2H<sub>4</sub>]pyrazine. *J. Chem. Soc., Faraday Trans. 2* **1985**, *81*, 405–415.
  - (55) Endrédi, H.; Billes, F.; Holly, S. Vibrational spectroscopic and quantum chemical study of the chlorine substitution of pyrazine. *Journal of Molecular Structure: THEOCHEM* **2003**, *633*, 73–82.
  - (56) Kearley, G.; Tomkinson, J.; Navarro, A.; López González, J.; Fernández Gómez, M. Symmetrised quantum-mechanical force-fields and INS spectra: s-triazine, trichloro-s-triazine and pyrazine. *Chemical Physics* **1997**, *216*, 323–335.
  - (57) Toma, H. E.; Malin, J. M. Properties and reactivity of some pentacyanoferrate(II) complexes of aromatic nitrogen heterocycles. *Inorganic Chemistry* **1973**, *12*, 1039–1045.
  - (58) Thompson, J. *Infrared Spectroscopy*; Jenny Stanford Publishing, 2018.
  - (59) Koishi, A.; Fernandez-Martinez, A.; Ruta, B.; Jimenez-Ruiz, M.; Poloni, R.; di Tommaso, D.; Zontone, F.; Waychunas, G. A.; Montes-Hernandez, G. Role of Impurities in the Kinetic Persistence of Amorphous Calcium Carbonate: A Nanoscopic Dynamics View. *J. Phys. Chem. C* **2018**, *122*, 16983–16991.